Received 14 June 2021; revised 27 October 2021, 5 February 2022, and 26 April 2022; accepted 5 May 2022.
Date of publication 29 July 2022; date of current version 22 February 2023.

Digital Object Identifier 10.1109/OAJPE.2022.3194865

Active Power Control of DFIG Wind Turbines for Transient Stability Enhancement

STAVROS KONSTANTINOPOULOS[1] (Member, IEEE)
AND JOE H. CHOW[2] (Life Fellow, IEEE)

[1]Grid Operations and Planning Group, Electric Power Research Institute, Palo Alto, CA 94304 USA
[2]Department of Electrical, Computer, and Systems Engineering, Rensselaer Polytechnic Institute, Troy, NY 12180 USA

CORRESPONDING AUTHOR: S. KONSTANTINOPOULOS (skonstantinopoulos@epri.com)

This work was supported in part by the Engineering Research Center Program of the National Science Foundation (NSF) and the Department of Energy (DOE) under NSF Award (EEC1041877) and in part by the Center for Ultra-Wide-Area Resilient Electric Energy Transmission Networks (CURENT) Industry Partnership Program.

ABSTRACT This paper proposes an adaptive Dynamic Power Reduction (aDPR) scheme for Type-3 Wind Turbine-Generators (WTGs) to enhance transient stability of synchronous generators (SGs), with benefits of increasing transfer limits on already fully loaded transmission paths. The scheme consists of three components to deal with a fault close to a SG. Initially, the WTG curtails its active power to a predefined level to act as a dynamic brake for the SG. Then the controller monitors the rate of change of frequency to adaptively ramp the WTG back to its original power output while minimizing the WTG pitch and rotor motion. Finally, to reduce the risk of second-swing instability, the converter uses its reactive current to damp SG power swings. The aDPR scheme can be classified as a remedial action scheme and is enabled if its action can ensure transient stability. To demonstrate the effectiveness of aDPR and to benchmark it against other WTG active current and frequency feedback control techniques, a single-machine infinite-bus system with one WTG is utilized. Next, an aDPR enabled WTG is integrated in the NPCC 68-bus system. Finally, the aDPR controller's ability to prevent transient instability is demonstrated on the two-area system.

INDEX TERMS DFIG, transient stability, renewable energy, wind turbine, remedial action scheme, active power control.

I. INTRODUCTION

INCREASED renewable energy source (RES) penetration will have profound impact on the reliable operation of future power systems. The current practice of renewable generation operating at maximum power generation, while providing a few grid support functions, such as low-voltage ride-through (LVRT) [1], [2], will soon be untenable. This paper further discusses the benefits of enabling active and reactive power control of RES, utilizing their low-inertia characteristics and fast-acting converters. Also motivated by fast control actions to achieve synchronization [3], this paper deals with transient stability enhancement by enabling a Type-3 WTG to perform fast active power control and act as a dynamic brake. Thus, in contrast to the increase of active power generation by the WTG to regulate against frequency drops [4], [5], this paper examines active power reduction to decrease the acceleration of a synchronous generator (SG) close to a severe fault. The WTG power then is recovered via an adaptive ramping scheme, achieved by estimating the acceleration of the SG using a phase-locked loop filter.

Transient stability is determined by the swing equation of the synchronous generator (SG)

$$2H\dot{\omega} = P_m - P_e - D\omega \tag{1}$$

where H is the inertia, ω the machine speed, P_m the mechanical input power, P_e the electrical output power, and D the damping constant of the SG. When the SG is subject to a short-circuit fault, ω accelerates and may cause the SG to be unstable. To restore transient stability, a control can either reduce P_m, like fast-valving [6], or increase P_e through controls employed on the network side. The latter can involve fast excitation system control, Flexible AC Transmission Systems (FACTS) controllers [7], plant tripping [8] and braking resistors [9].

In this paper, we develop an active power control scheme for the WTG to provide transient stability enhancement by increasing the P_e term of the SG without needing expensive

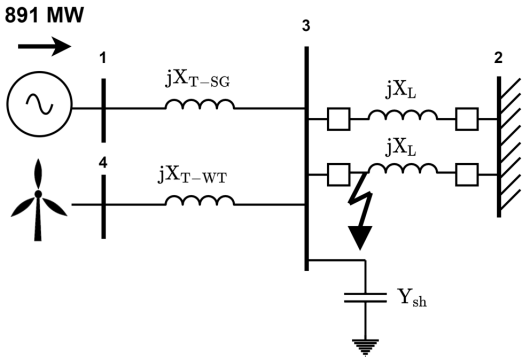

FIGURE 1. **Single-machine infinite-bus and wind-turbine system.**

network transmission enhancement. The motivating scenario is the single-machine infinite-bus (SMIB) system shown in Fig. 1, in which the SG on Bus 1 is already transmitting the largest allowable amount of power to the infinite bus for a specific Critical Clearing Time (CCT). The problem to be investigated is, if a nearby quality wind site is to be utilized for a WTG installation and the additional power is to be transferred to the infinite bus. We investigate whether the new WTG can utilize the same transfer path to provide power to the infinite bus, without lowering the CCT of the SG subject to a severe disturbance such as a short-circuit fault near Bus 3 and cleared by removing one of the lines connecting Buses 3 and 2 (Fig. 1). The first-swing stability of the SG can be enhanced if the WTG control can increase the P_e extracted from the SG when the SG is accelerating.

Various open- and closed-loop active power control schemes have been proposed by researchers. The Low Voltage Power Logic (LVPL) function provided by WTG manufacturers [10] can provide transient stability improvement with active power limitation. However, with the recommended settings, if the voltage recovers immediately after a fault, the transient stability benefits can be minimal. Ref. [11] examines active power current curtailment of wind plants, based on simulation derived sensitivity factors. Beneficial reactive power injections are determined with a similar approach. The authors demonstrate the superior performance of coordinated curtailment compared to the LVPL function. Ref. [12] utilizes a zero dynamics approach for transient stability improvement utilizing wind farms. Ref. [13] utilizes reinforcement learning for wide-area transient stability control using WTGs. During disturbances, [14] uses a frequency feedback control implemented in the torque command of the WTG to adjust its active power output. Ref. [15] proposes a supplementary active power controller for transient stability enhancement, using a derivative filter. In [16] fuzzy logic nonlinear/adaptive current limiters are used to enhance the transient stability of a SG-photovoltaic-WTG system. Ref. [17] implements a Proportional Integral (PI) WTG rotor speed deviation feedback in the electrical torque command of the WTG to operate it as a motor to absorb power from adjacent accelerating generators in disturbance conditions. In [18], the authors utilize linear feedback control for active and reactive current transient stability control. The reactive current gain is calculated to maximize active power and ensure a valid equilibrium point for the PLL. The active power feedback utilizes PI feedback of the PLL frequency with a deadband. The controls mentioned above either directly control the converter active power current output or change the WTG torque command. These controls can demand large injections or extractions of energy from the WTG rotor, which may cause large undesirable speed deviations. However, the proposed design in this paper achieves transient stability improvement while minimizing pitch actuation and rotor speed deviation. Ref. [19] examines the effect of active power injections of WTGs, on transient stability by utilizing the Extended Equal Area Criterion (EEAC). Based on the derived conditions, active power setpoints are calculated for each swing, ensuring transient stability improvement.

The proposed adaptive Dynamic Power Reduction (aDPR) controller adds the power reduction control to the WTG power-order setpoint input, thus allowing the turbine blades to pitch and regulate rotor acceleration. The proposed control consists of three parts: (1) a dynamic power reduction scheme for the WTG to act as a braking resistor to slow down the SG acceleration, (2) an adaptive ramping control back up to the WTG's original power level, and (3) a damping controller using the converter's reactive current output to minimize subsequent power swings. The design here accounts for the wind hub rotor dynamics to optimize the blade pitch angle and rotor speed deviations. To illustrate the benefits of the proposed approach, a comprehensive comparison to the LVPL and frequency feedback control [14] is included. In addition, the applicability of the proposed control scheme in a multi-machine power system and the two-area system is demonstrated.

The remainder of the paper is organized as follows. Section II describes a generic Type-3 WTG model and Section III the proposed aDPR control. Section IV illustrates the performance of the aDPR scheme in a SMIB system (Fig. 1) and compares it against other methods. Section V extends the testing to the NPCC 68-bus system and Section VI to the two-area system.

II. TYPE-3 WTG MODEL

The block diagram of the Type-3 WTG model and its controls based on [10] is shown in Fig. 2. The model of each block is described as follows.

1) WTG ROTOR DYNAMICS

The rotor dynamics of a one-mass WTG model representing the hub, gearbox, and induction generator rotor is modeled by

$$\Delta\dot{\omega}_G = \frac{1}{2H_g}\left(\frac{P_{mech} - P_G}{\omega_0 + \Delta\omega_G}\right) \tag{2}$$

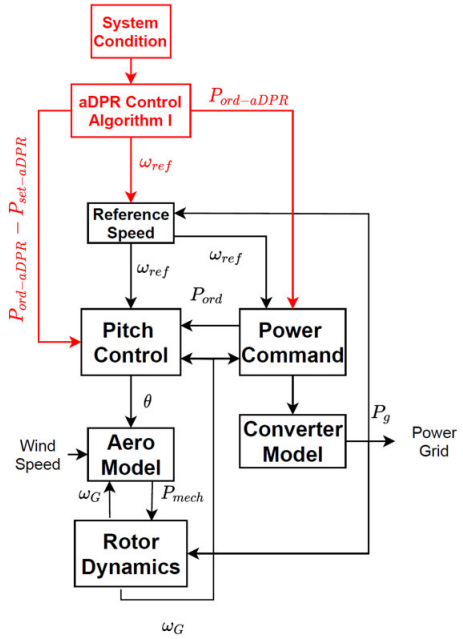

FIGURE 2. **WTG active power control loops and aDPR integration. The reactive power control of aDPR is shown in Fig. 6.**

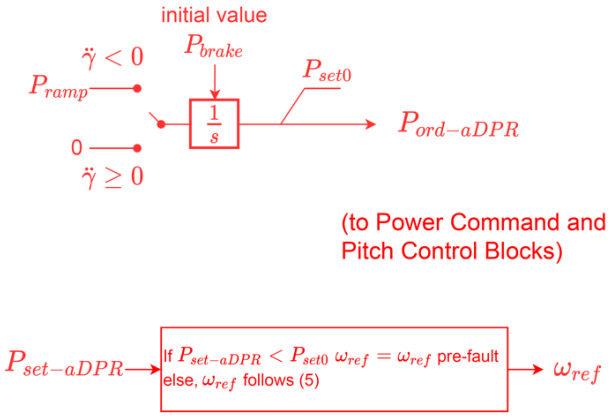

FIGURE 3. **aDPR block diagram logic.**

where $\Delta\omega_G$ is the rotor speed deviation from the nominal speed ω_0, P_{mech} is the wind power captured as mechanical input power to the rotor, P_G is the active power output of the induction generator and H_g is the inertia constant of the rotor mass. The mechanical power input P_{mech} to the rotor is determined by the aero model.

2) AERO MODEL

The aero model determines P_{mech} as a nonlinear function of the wind speed and the pitch angle based on a measured wind power conversion table [10]. An example two-dimension power surface can be found in [21].

3) PITCH ANGLE DYNAMICS

Using the error functions

$$\dot{\delta}_{err1} = K_{ip}\Delta\omega_{G1},\ \dot{E}_{err} = P_{err} = P_{ord} - P_{\text{set}} \tag{3}$$

where δ_{err1} is the angle error due to the rotor speed deviation, $\Delta\omega_{G1}$ is the rotor speed deviation from the reference speed, P_{err} is the power command error towards the setpoint P_{set} and E_{err} is the energy error towards the power setpoint. The pitch angle θ is controlled by

$$\dot{\theta} = \frac{1}{T_p}\left[-\theta + K_{pp}\Delta\omega_{G1} + \delta_{err1} + K_{pc}P_{err} + K_{ic}E_{\text{err}}\right] \tag{4}$$

where T_p is the pitch angle time constant, K_{pp} and K_{ip} are the proportional-integral (PI) gains of the WTG's rotor speed deviation from the reference speed, respectively, and K_{pc} and K_{ic} are the PI gains, respectively, for the power error towards the set-point.

4) POWER COMMAND DYNAMICS

The active power command P_{ord} is computed from

$$\begin{aligned}\dot{P}_{ord} &= \frac{1}{T_{pc}}\left(-P_{ord} + \omega_G(K_{ptrq}\Delta\omega_{G1} + \delta_{err2})\right)\\ \dot{\delta}_{err2} &= K_{itrq}\Delta\omega_{G1}\end{aligned} \tag{5}$$

where K_{ptrq} and K_{itrq} are the PI torque command gains, respectively, for the speed deviation and T_{pc} is the time constant of the power command.

5) REFERENCE SPEED DYNAMICS

The reference WTG rotor speed ω_{ref} is obtained from the nonlinear differential equation optimized with respect to the active power output P_G [20]

$$\dot{\omega}_{ref} = \begin{cases} \dfrac{1}{T_{d\omega}}(1.2 - \omega_{ref}) & \text{if } P_G \geq 0.46 \\ \dfrac{1}{T_{d\omega}}(-0.75P_G^2 + 1.59P_G & \\ +0.63 - \omega_{\text{ref}}) & \text{if } P_G < 0.46 \end{cases} \tag{6}$$

where $T_{d\omega}$ is the reference speed dynamics time constant.

6) CONVERTER DYNAMICS

The active power part of the converter current I_p output is computed as

$$\dot{I}_p = \frac{1}{T_{ddel}}\left(\frac{P_{ord}}{V_t} - I_p\right) \tag{7}$$

where T_{ddel} is the converter time constant. The Phase-Locked Loop (PLL) angle γ, tracking the converter or point-of-interconnection bus angle θ, is modeled as [25], [26]

$$\dot{\gamma} = K_{pllp}V_t\sin(\theta - \gamma) \tag{8}$$

where V_t is the bus voltage magnitude and K_{pllp} is the PLL control gain. In addition, $\dot{\gamma}$ is an estimate of the terminal bus frequency.

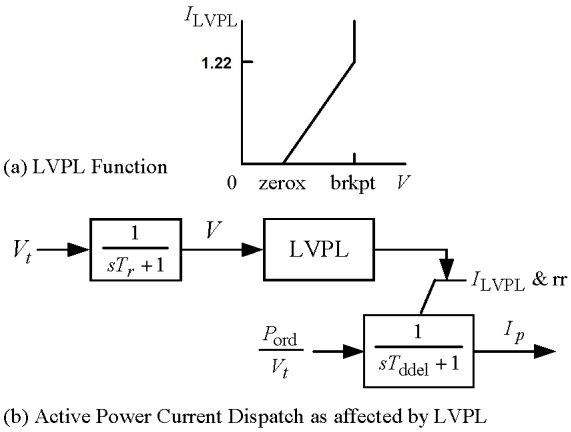

FIGURE 4. **Low value power logic (LVPL) block diagram.**

In low-voltage conditions, the LVPL logic and current limiting function shown in Fig. 4 [10] can be activated with a time constant T_r, by the filtered terminal voltage dropping below V_{brkpt}. The LVPL calculates the limit applied on I_p and recovery is dictated by a ramp rate limit rr, which is enforced even if the voltage recovers, until the plant reaches steady state. The limits are subject to tuning in order for certain voltage ride-through or transient stability specifications to be met.

In the phase II generic models [22], freezing P_{ord} and the T_{ord} integrator, when a voltage dip is detected, was introduced. We will introduce this integrator freeze for the time I_p takes to recover due to the slow current ramping that will be enforced in later sections, as it allows the pitch controller to actuate more effectively and makes the comparison of the controls more illustrative. In our proposed design, the LVPL controller is replaced by the aDPR. The models were implemented in the Power System Toolbox [24] as described by [25], [27], which is utilized for dynamic simulation and linear analysis.

III. THE aDPR CONTROLLER INTEGRATION

The implementation of the aDPR as a control block in the overall active power WTG control is shown in Fig. 2. The three components of aDPR in the context of Fig. 1 are described as follows.

7) DYNAMIC POWER REDUCTION

The basic feature of the aDPR is the fast reduction of the active power output level to P_{brake}, which could be 10-50% of the pre-fault active power output level presented in [28]. After the fault is cleared, the power is ramped back up to the pre-fault power level at a constant rate of P_{ramp}. The control is shown in Fig. 3 and enumerated in Algorithm 1.

Upon the detection of a fault condition indicated by low voltage at the point-of-connection bus, the internal state (integrator) of the aDPR is reset to P_{brake}. As the fault is cleared, the output of the integrator is increased at a rate of P_{ramp}.

Algorithm 1 aDPR Control Logic

if Fault On Condition **then**
  $P_{set} = P_{ord} = P_{brake},\ \dot{P}_{ord} = 0,\ \omega_{ref} = \omega_{ref0}$
else if Transient Condition & $P_{set} < P_{set0}$ **then**
  $\omega_{ref} = \omega_{ref0}$
  if $\ddot{\gamma} < 0$ **then**
    $\dot{P}_{ord} = \dot{P}_{set} = P_{ramp}$
  else
    $\dot{P}_{ord} = \dot{P}_{set} = 0$
  end if
else
  $\dot{P}_{ord} = f(P_{ord}, \omega_G, \omega_{\text{ref}}, \delta_{err})$
end if

If SG acceleration is sensed via the monitoring of $\ddot{\gamma}$, the ramp is paused, via setting the input of the integrator to zero. The ramp has an upper limit at the original power set-point. When that point is reached, or the system settles to steady state before that, the aDPR control is deactivated. The derived output set-point and power command, denoted as $P_{set-aDPR}$ and $P_{ord-aDPR}$, are then used in the pitch and power command loops. Specifically, the power command loop is overridden by the aDPR command, while the pitch control loop utilizes the dynamics of eq. (4), while utilizing the aDPR derived quantities.

By running back the WTG output, additional electrical power will be demanded from the SG, thus speeding up the deceleration of the SG rotor. In this sense, the concept is similar to the LVPL, except that the power reduction and subsequent ramping is commanded through P_{ord} and P_{set}. In contrast, the LVPL directly commands the converter output current, I_p, to achieve fast response, without any internal mechanical or electrical variable considerations. The proposed power reduction goes through the setpoint/power command, which allows the pitch controller to actuate more effectively, achieving smaller $\Delta\omega_G$ deviation than the LVPL. In addition, curtailment through the power command reduces significantly output power oscillations caused by voltage fluctuations, especially when the WTG is connected to a weak and stressed system in contrast to the LVPL that was observed to introduce oscillations [23].

8) ADAPTIVE RAMPING

The efficacy of the ramping control can be improved by sensing the acceleration of the SG which the controller is stabilizing. With fast WTG power reduction, the synchronous machine will experience a faster deceleration. As soon as acceleration is observed, the ramp freezes in order to not exacerbate the rotor acceleration and cause second-swing instability. The switching logic is implemented by setting the input of the integrator in Fig. 3 to zero.

This pause can be triggered by measuring the SG rotor speed. However, doing so requires transmitting the SG speed to the WTG controller through some dedicated

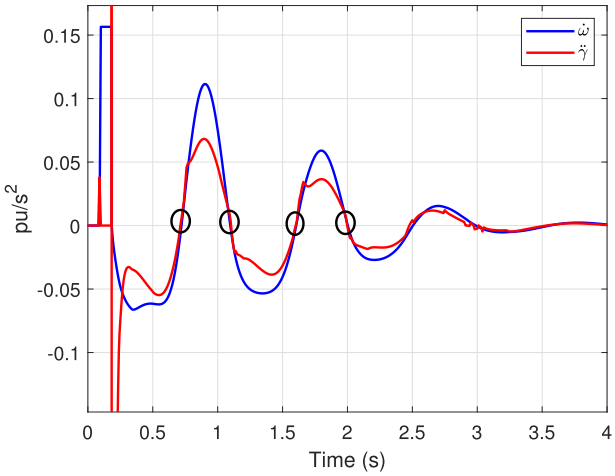

FIGURE 5. SG acceleration and $\ddot{\gamma}$ after 3-phase fault.

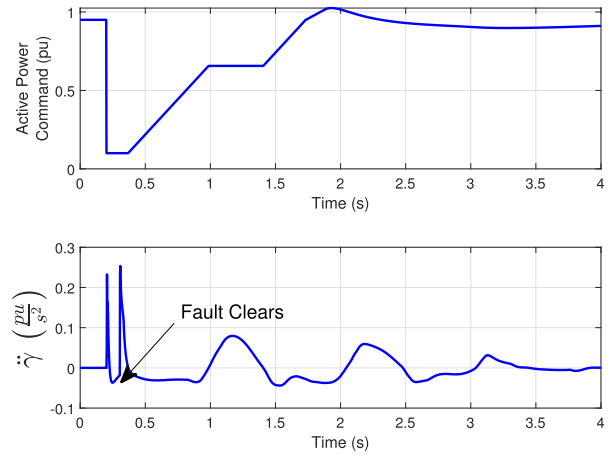

FIGURE 6. aDPR ramping profile for adjacent bus 3-phase fault.

communication link. In this work, the second derivative of the PLL angle $\ddot{\gamma}$ can be used as a local estimate of the Rate of Change of Frequency (ROCOF) of the WTG bus, which correlates well with the SG acceleration. For illustration, the acceleration of the SG and the second derivative of the PLL angle, are presented in Fig. 5, for the SMIB system. The two signals present high correlation, and most importantly have common zero-crossings. The zero-crossing points are relevant, since they are utilized by our control to initiate and pause the adaptive ramp and alleviate the risk of second swing instabilities.

To illustrate the first two components, the active power ramping profile of the WTG is shown in Fig. 6 when the disturbance event is applied on Bus 3 of the SMIB system. At the onset of the fault on Bus 3, the WTG reduces the active power output from 0.95 pu to 0.1 pu. When the fault is cleared. The WTG power is ramped back up at a rate of 0.9 pu/s. At t about 1 s, $\ddot{\gamma}$ becomes positive, triggering the pause in the power ramp. The ramp restarts at t about 1.4 s when $\ddot{\gamma}$ becomes negative. The ramp input stops when the WTG power reaches back to 0.95 pu, after which other active power control takes over. Since the proposed active power control is designed on an aggregate model of the wind farm, when applied, it should be realized in the plant-level controls. The control effort distribution will be based on each WTG's individual loading and its ability to reduce its output to achieve the overall desired control objective. In addition, the active power component of aDPR has two tunable parameters, namely, P_{brake} and P_{ramp}. As with the LVPL, these values were tuned via simulation, in order to achieve the required transient stability margins.

9) REACTIVE POWER CONTROL COORDINATION

Because of the importance of reactive power support in the immediate post-fault period, the WTG will be put in the Q-priority control. Given the headroom created by the active power curtailment of the WTG plant post-fault, reactive power can be controlled to damp the SG swings without the risk of the WTG being constrained by current limitations.

The reactive power control can be summarized as

$$\dot{E}_{fd} = \frac{1}{T_{ddel}}(E_{fdcmd} - E_{fd} + u_D) \tag{9}$$

$$\dot{E}_{fdcmd} = K_{Vi}(V_{ref} - V_t) \tag{10}$$

$$\dot{V}_{ref} = K_{Qi}(Q_{ord} - Q_G) \tag{11}$$

where E_{fd} is a voltage behind the reactance X_{pp}, E_{fdcmd} is the voltage command, V_{ref} is the synthesized voltage reference, Q_{ord} is the reactive power command, V_t is the terminal voltage, Q_G is the reactive power output, u_D is an input for damping control, and K_{Vi} and K_{Qi} are the terminal bus voltage and reactive power regulator gains, respectively.

The reactive power command dynamics are modeled by

$$\dot{s}_3 = \frac{1}{T_r}(V_{reg} - s_3) \tag{12}$$

$$\dot{s}_4 = V_{rfq} - s_3 \tag{13}$$

$$\dot{s}_2 = \frac{1}{T_V}(V_{rfq} - s_3 - s_2) \tag{14}$$

$$\dot{Q}_{ord} = \frac{1}{T_c}\left(K_{iv}s_4 + K_{pv}s_2 - Q_{ord}\right) \tag{15}$$

where s_4 integrates the error of the filtered regulated voltage s_3 towards the reference. The regulated voltage is filtered by a transducer with time constant T_r. V_{rfq} is the reference voltage. K_{pv}, K_{iv} are the PI gains that dictate the reactive power command Q_{ord}. The proportional part of the control is filtered by a time constant T_V. The reactive power command dynamics have a time constant T_c. A PI damping control u_D is implemented as shown in Fig. 7. The input is $\dot{\gamma}$, the PLL's estimate of frequency, which is passed through a low-pass filter with a time constant T_{LP}. The integral gain K_i and the proportional gain K_p are tuned to provide positive damping for the SG swing mode [21], while still supporting the voltage in transient conditions. The parameter values are given in the Appendix. The proportional gain of the control provides a fast reactive power injection immediately after the fault is cleared,

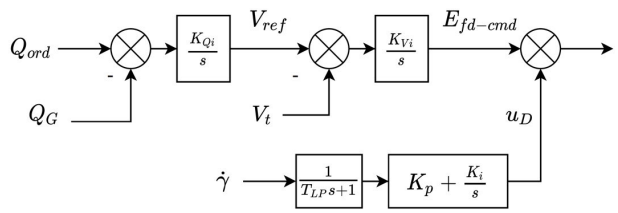

FIGURE 7. Reactive power PI damping controller and its integration in reactive power control loops.

utilizing the current headroom created by the curtailed active power. The integrator serves two purposes. It provides a quick bias correction to E_{fd} based on the accelerating angle and provides lag to improve the electromechanical swing damping similar to a design in [29].

The output of the PI controller is then superimposed to synthesized E_{fdcmd} as depicted in Fig. 7. The damping control signal is limited to ± 0.5 pu. Finally, Q priority is assumed, so if the total current exceeds the limit, I_p will be curtailed accordingly.

If the power ramp was tuned appropriately, the second swing of the SG rotor angle should be well damped. If the second swing reached the same peak angle value as the first, the system would go unstable (in the marginally stable case). This highlights the importance of effective damping of the power swings. Alternatively, one could tune the ramping of the WTG to a lower value and alleviate this second swing problem. However, prolonged curtailment, despite the optimized design of the aDPR, will force the rotor and the pitch to move significantly. We adopt a PI design which for our purposes is sufficient. In cases of multiple plants or if additional feedback signals are available, more sophisticated design techniques can be utilized.

For control tuning, various approaches can be carried out. For our purpose we adopt a phase compensation design [21] similar to one used for static var systems, which uses phase lag to achieve good damping performance. In our design, the required lag compensation at the swing mode frequency is provided by the PI regulator by setting $K_p/K_i = 0.1$. We then choose an appropriate gain using the root-locus technique. An example of the uncompensated and compensated root-locus plots can be noted in Fig. 8.

10) CURRENT INJECTION

After all the control actions, the converter is interfaced with the network as a current source with the terminal current injection being [27]

$$\tilde{I} = \left(I_p - j\frac{E_{fd}}{X_{pp}}\right)e^{j\gamma} + j\frac{Ve^{j\theta}}{X_{pp}} \tag{16}$$

If a PLL is not present in the model, the angle used for the injection (i.e. γ) is the bus voltage angle.

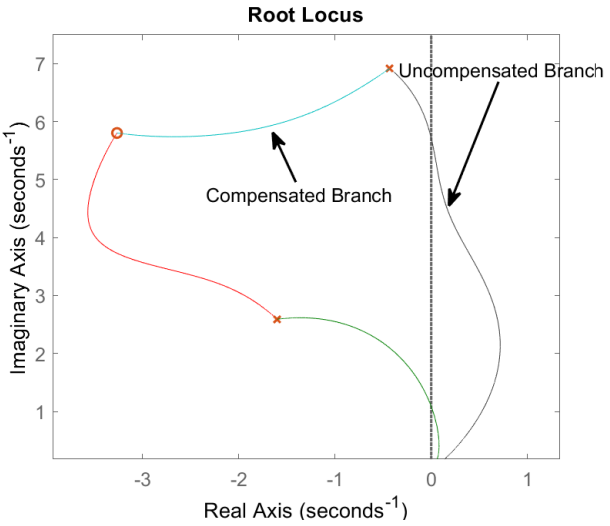

FIGURE 8. Root-locus plots around swing mode for uncompensated and compensated system.

IV. SMIB AND WIND-TURBINE SYSTEM

The SMIB system with a WTG of Fig. 1 is used to show that the aDPR control of the WTG allows additional power transfer on an already congested transmission path from Buses 3 to 2.

A. SYSTEM DESCRIPTION

The SG is connected via a transformer to a high-voltage bus. Two parallel lines connect the transformer to the infinite bus, modeling the bulk system. The limiting $N-1$ contingency is a three-phase fault on Bus 3, followed by the tripping of one of the two parallel lines. Now we consider the installation of a WTG plant. It would be desirable to utilize the existing transmission infrastructure, avoiding extra investments. The aggregate WTG is thus connected at its point-of-interconnection (Bus 4) to the high-voltage bus (Bus 3) via a step-up transformer. A capacitor bank is added at Bus 3 for voltage support, due to the additional power transfer. The two transmission lines have a reactance of 0.056 pu each, on a 100 MVA base. The reactances of the SG and WTG transformers are 15% on their respective generator bases. The SG is rated at 991 MVA and is loaded to 90% (891 MW) of its rating. It is equipped with a first-order excitation system and a power system stabilizer. Additional data for this system is provided in the Appendix. Without the WTG, the critical clearing time (CCT) of the SG for this limiting contingency is 5.5 cycles. With the installed WTG plant supplying 200 MW (95% of rating), the CCT deteriorates to 4.5 cycles due to the additional flow to the infinite bus, with the WTG not providing any active power control.

B. SYNCHRONOUS GENERATOR WITH WIND TURBINE ON aDPR CONTROL

The aDPR is now applied to the WTG with parameters $P_{brake} = 0.1$ pu and $P_{ramp} = 0.9$ pu/sec. The SG response due the limiting contingency with a clearing time of 6.3 cycles

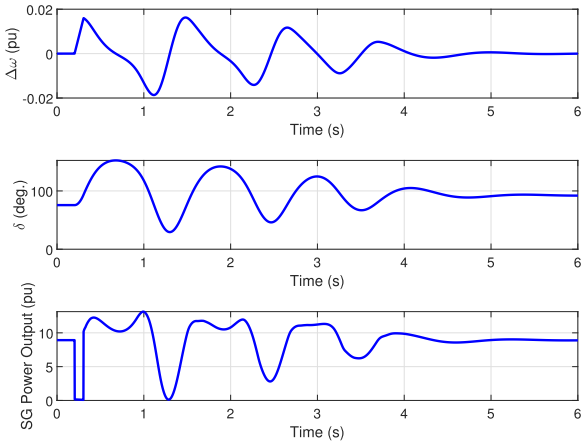

FIGURE 9. Synchronous generator speed, rotor angle and active power output for a 3-phase fault on bus 3.

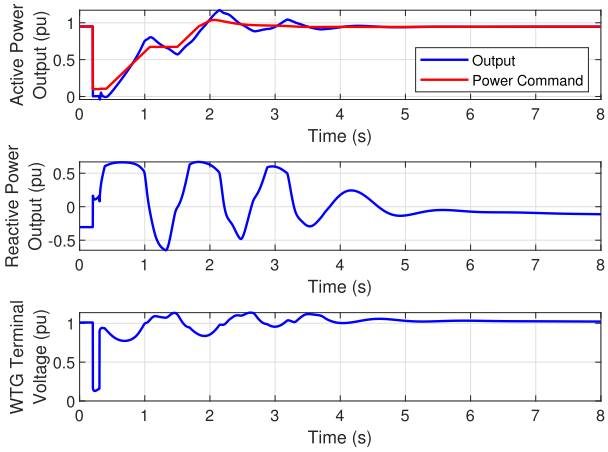

FIGURE 10. Wind turbine-generator active and reactive power, and terminal voltage for a 3-phase fault on bus 3.

is stable, as shown in Fig 9. The oscillations following fault clearance subside in about 4 sec. During the first swing, the suppressed power output of the WTG forces the SG to provide additional active power to the infinite bus, including the share previously supplied by the WTG.

Figs 9, 10 show the interplay between active power outputs of the SG and the WTG. As the SG rotor angle δ increases, the SG power output would also increase. However, as the WTG output power ramps up, the SG output power would decrease. The SG rotor speed continues to decrease until about 1 sec when $\dot{\omega} = 0$. At this time, the ramping of the WTG is paused. Slightly after 1 sec, the output power of the SG drops to near zero, even though δ is higher than the infinite-bus angle, which is fixed at 0°. This is due to the WTG supplying all the line power flow by itself. The WTG power ramping would restart when ω reaches a maximum again at about 1.4 sec.

Figure 10 depicts the detailed WTG response for the simulated fault. The WTG reaches the pre-fault output in 1.8 sec. The ramping is fast but yet would not put much stress on the mechanical actuation (as shown later). The pause in

TABLE 1. Comparison of CCTs for active, reactive and combined aDPR controller components.

Active Controls	Basic	Active Power Control	Reactive Power Damping Control	aDPR
CCT (cycles)	4.5	6	4.85	6.3

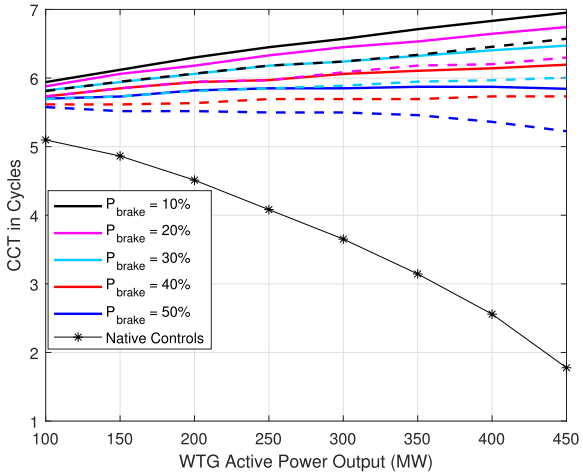

FIGURE 11. Stability margin for various WTG output levels and braking power levels. Solid lines—aDPR control; dashed lines—without Q damping control.

ramping between 1 and 1.4 sec can be noted in the power command plot. While the WTG active power is curtailed, it is providing higher reactive power support to the grid, and as a result reduces the variation of the WTG terminal bus voltage. Finally, to highlight the efficacy of the active power control of the aDPR's design, we compare the CCTs of the basic controls, aDPR using only the active power, aDPR using only the reactive power damping controller, and aDPR using all three components. The results are summarized in Table 1. The damping control, when acting alone, provides only 0.35 cycles of CCT improvement. As the active power recovers immediately after the fault is cleared, the voltage state is saturated attempting to support the voltage, leaving little room for transient reactive power control.

C. STABILITY MARGIN FOR DIFFERENT RENEWABLE PENETRATION LEVELS

To systematically assess the benefit of the aDPR control, the CCTs for the same disturbance are computed for various WTG output and P_{brake} levels. For each case an aggregate WTG with the described output is installed at the same location, and the x-axis power output corresponds to 95% of its rated power. The resulting CCTs are plotted in Fig. 11. Note that without the aDPR control, the CCT decreases quite rapidly. With the aDPR control, the CCT mostly improves as the WTG output increases, particularly at low P_{brake} levels. This is to be expected given the decelerating mechanism that the aDPR exploits. Even without the reactive power

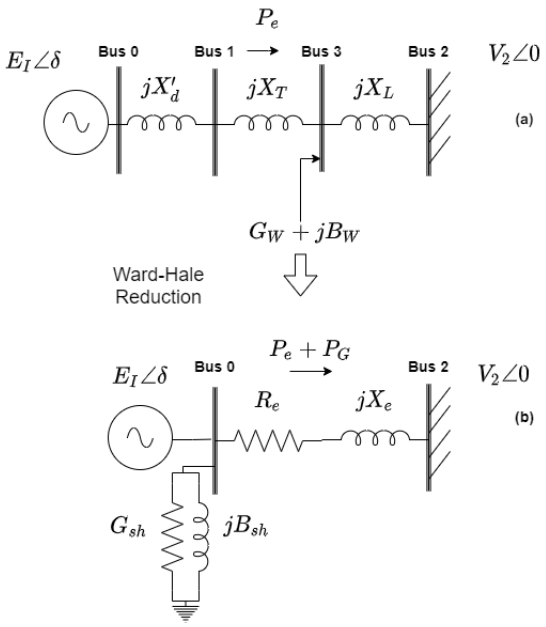

FIGURE 12. Reduced admittance representation incorporating WTG effect.

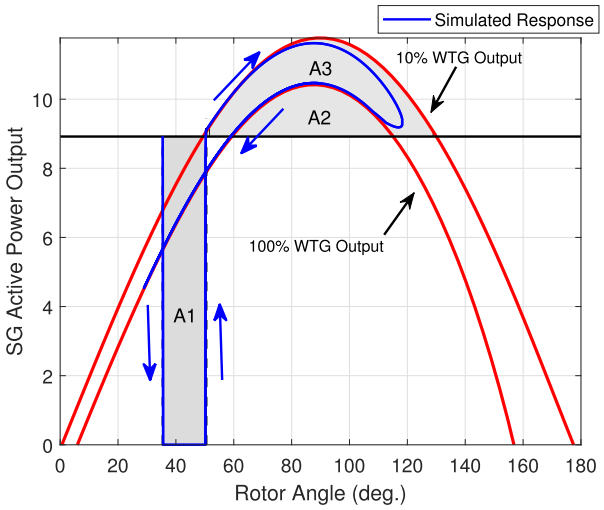

FIGURE 13. SG power angle curve and equal area criterion for 200 MW WTG full and curtailed active power output.

damping control component, the CCT can be maintained for $P_{brake} \leq 40\%$.

D. SYNCHRONIZING TORQUE BENEFIT OF aDPR

The merits of the aDPR in improving the synchronizing torque and hence the transient stability margin can be illustrated graphically using the equal-area criterion (EAC) idea. To use the EAC, the post-fault system with one line between Buses 2 and 3 removed is simplified with the WTG power injection into Bus 3 modeled as a negative load $G_W + jB_W = (P_W + jQ_W)/V_{3o}^2$, where V_{3o}^2 is the initial voltage magnitude on Bus 3 (Fig. 12a). Applying the Ward-Hale network reduction process [21], the circuit can be reduced to the system depicted at the bottom of Fig. 12 where Bus 0 denotes the SG internal voltage node behind the transient reactance X'_d, and the negative load $G_W + jB_W$ represents the WTG injection.

Thus the total power flowing through the equivalent line can be rewritten as

$$P = E_I V_2 G_e \cos\delta + E_I V_2 B_e \sin\delta + G_{sh} E_I^2 \qquad (17)$$

where $G_e + jB_e = -1/(R_e + jX_e)$. Since the WTG is represented by a negative load, G_{sh} must be negative to keep the power flows between the two systems the same. Thus, the equivalent dynamics of the reduced system are

$$2H\dot{\omega} = P_m - E_I V_2 G_e \cos\delta - E_I V_2 B_e \sin\delta - G_{sh} E_I^2 \qquad (18)$$

The two additional conductances represent the effect of the WTG power injections first by increasing the effective resistance between Buses 0 and 2 (angle dependent component) and second by applying a direct shunt injection on the internal node of the SG. This injection acts as an active power "bias" which has to flow through the transmission line, effectively pre-loading it. Thus, the curtailment of power reduces the value of G_{sh}, i.e., decreasing the shunt injection and improving synchronizing torque. This is captured in the $P-\delta$ curves of Fig. 13 of the circuit in Fig. 12(b), for 100% and 10% WTG power output. Because of the WTG power injection, these power curves do not start from the origin. For example, if the WTG is supplying 100% of its rated active power to Bus 2, the angle at Bus 3 is 6.5°, which is equal to δ although the SG is unloaded. This has the effect of pushing the $P-\delta$ curve down and reducing the area (A2 in Fig. 13) between it and P_m, the rated SG power output, and thus the synchronizing torque. When the WTG output power is temporarily curtailed, the $P-\delta$ curve rises to increase its area between P_m, denoted by A3, and restore the synchronizing torque. In addition, during the active power curtailment, the WTG can provide additional capacitive power, further improving the synchronizing torque.

Also note that in contrast to the traditional $P-\delta$ curve which is symmetric about $\delta - \theta_3 = 90°$, the curves in Fig. 13 does not exhibit the usual symmetry property. For further illustration, the SG disturbance response is superimposed on the power angle curves of Fig. 13. Initially, the WTG output power is curtailed to 10%, thus, the response follows the 10% WTG power $P-\delta$ curve and gradually approaches the fully loaded $P-\delta$ curve as the WTG power is restored. As an illustration, the acceleration of the SG is plotted for various power braking levels in Fig. 14. The synchronization can be noted to deteriorate as the braking power increases.

E. COMPARISON WITH OTHER ACTIVE POWER CONTROL METHODS

The aDPR scheme is now compared to two other schemes mentioned in Section I. First, the LVPL scheme [10] limits I_p directly. The ramp limit was tuned to 0.3 pu/sec to achieve

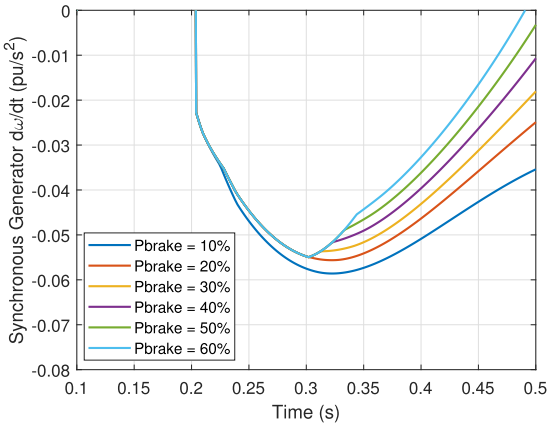

FIGURE 14. Acceleration of SG for various P_{brake} levels.

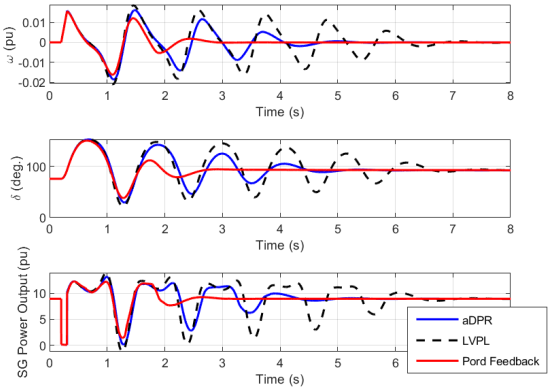

FIGURE 15. Synchronous generator speed, rotor angle and active power output for a 3-phase fault on bus 3, for various control schemes.

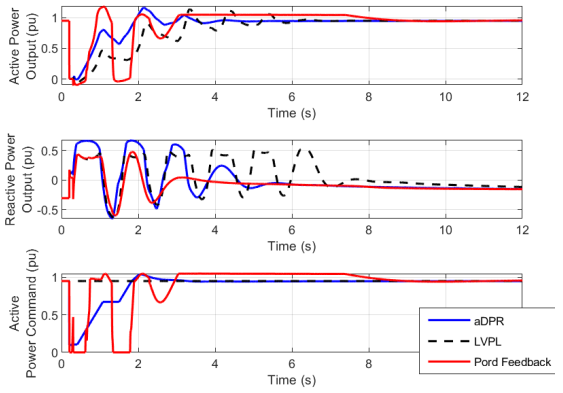

FIGURE 16. Wind turbine generator output power and command for various control schemes.

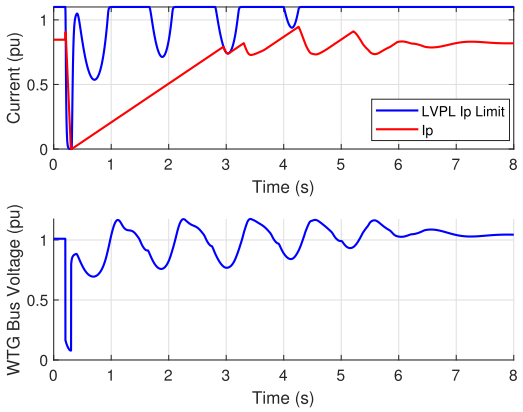

FIGURE 17. I_p, LVPL I_p limit and WTG terminal voltage for 6.2 cycle fault on bus 3.

a CCT of 6.2 cycles. Second, the connection bus frequency feedback control of [14] is superimposed onto P_{ord}. Only the proportional part of the proposed PI control was used. The integral gain of the control was not utilized as it did not yield a higher CCT or better damping performance, while resulting in longer zero active power output periods for the WTG, resulting in more mechanical actuation. The maximum achievable CCT (without severe reverse power flows into the WTG) was 6.1 cycles. The gain for negative proportional feedback was tuned to 377 pu-power/pu-frequency and is activated for 2 seconds following the fault due to its very high gain. To make the comparison between the controllers more consistent, the ω_{ref} dynamics are frozen. The SG responses for these controls are shown in Fig. 15. The LVPL scheme appears to have the worst damping performance, with oscillations persisting up to 6.8 sec, while the feedback control achieves the best damping of the swings. In addition, on the downward swing, the LVPL causes negative power flow on the SG, due to the prolonged curtailment and insufficient swing damping.

The WTG responses are shown in Fig. 16. The feedback control with the high gain ramps the power output down to 0% and back up to 100% twice. This action causes high power extractions and injections into the WTG. The resulting energy mismatches in the internal loops of the WTG are evident, since the active power remains at its maximum for a prolonged period in order to rectify these accumulated errors. On the other hand, the LVPL gradually ramps up the active power current, and the current limitation only comes into effect on the third swing, as shown in Fig. 17. Finally, the dominant component of the LVPL in this case is the ramp limiter, which forces the WTG into a linear ramp back to pre-fault set-point. However, in transient conditions, the electromechanical swings of the SG will produce voltage oscillations, which when multiplied by the linear active current ramp of the WTG will produce oscillatory active power injections, which in turn worsen the post-fault response of the system.

Next the impact of these controls on the mechanical components of the WTG is investigated. Fig. 18 shows the pitch angle and the WTG speed deviation in the post-fault period. The LVPL control forces the pitch angle to increase by 7° in order to counter the rotor acceleration due to the active power

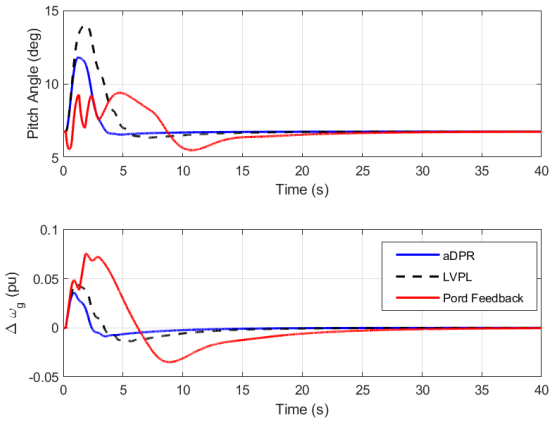

FIGURE 18. Wind turbine pitch angle and rotor speed for various control schemes.

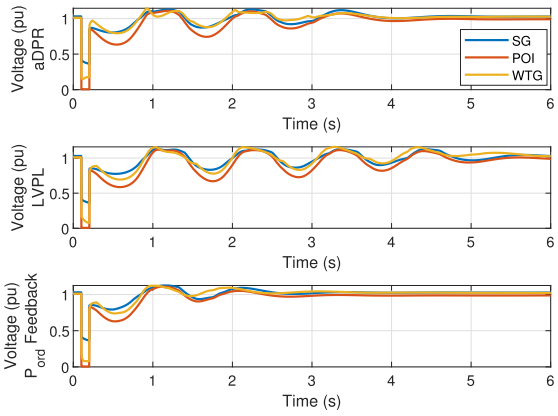

FIGURE 19. System voltage profile for compared controls.

curtailment. Due to the very slow ramping and oscillating power output the pitch takes 5 sec. to settle.

On the other hand, the P_{ord} feedback does not force the pitch to actuate in as wide a range, but uses the rotor inertia as a buffer for exchange of power with the grid. However, due to the rapid changes of power output, the pitch is forced to ramp up and down until the transient controller is deactivated in 2 s. These power exchanges result in the rotor taking 25 s to settle back to its reference value. Comparatively, the aDPR requires 5° of pitch response, with a peak acceleration of 2%. This is achieved by the faster power ramping and the curtailment through the power command.

Finally, the effect of each control on the system's voltage profile are shown in Fig. 19. As noted, the aDPR active and reactive power components achieve better voltage profile for the transient period compared to the LVPL and for the first swing compared to the frequency feedback. As a result, the aDPR enhances the voltage ride-through capability of the system.

V. NPCC 68-BUS SYSTEM

The NPCC 68-bus system [30] in Fig. 20 is used to test the aDPR in a multi-machine setting. In this system, SG 9 on Bus 61 has a CCT about 5 cycles when one of the lines connecting it to the main system is faulted and cleared. A WTG rated at 210 MVA with output of 200 MW is connected to Bus 29, through a transmission line with a reactance of 0.1 pu and a transformer with a reactance of 15% on the WTG base. A load is added on Bus 28 to consume the wind energy, thus increasing the loading on the lines connecting to the main system.

The first disturbance being considered is a three-phase short-circuit fault on Bus 29 and cleared by opening Line 29-28. The CCT for this contingency is 4.2 cycles, with the WTG operating without active power control. The instability in this case is SG 9 separating from the system. With aDPR the CCT increases to 7.2 cycles. Here the aDPR uses the same parameters as the SMIB case. The generator response to the disturbance at 7.2-cycle clearing time is shown in Fig. 21. Following fault clearing for the no aDPR case, the SG 9 rotor speed does not return to 1.0 pu, resulting in instability. Note that only 3 s of simulation is shown for this unstable case. On the contrary, when the aDPR is activated, the SG 9 power output persists above the steady-state value for 1 s, allowing sufficient time for its rotor to decelerate. Thus, SG 9 stays in synchronism. Fig. 22 shows the response of the WTG with and without the aDPR. The active power output in this case is curtailed for close to 3 s following the fault.

To show that the aDPR control is applicable to other fault conditions, the improvement in CCT for additional 3-phase short-circuit faults is tabulated in Table 2. Three different load placements are considered. The first column indicates what line is tripped and which bus is the fault applied on. For example line 29-28 means that the fault is applied on Bus 29. The other columns indicate the bus with the load increase, and the corresponding CCTs. The CCTs are in cycles and the CCT values in parentheses are without aDPR. In all cases, P_{brake} is set to 0.1 pu. Overall, the aDPR offers good improvement of CCTs across all cases, with an average of about 2 cycles. In particular, those cases with CCT raised to above 5–6 cycles are important because protective relays readily have such capability.

We then consider an alternative scenario. The WTG is placed on Bus 26, rated at 400 MW and supplying a 400 MW load on Bus 27. The contingency considered is a three-phase short-circuit fault on Bus 25, followed by a trip of line 25-2. This forces the power from generator G8 to flow solely on line 26-27 that is also utilized by the newly installed WTG. The SG speeds for the case, with and without aDPR, can be noted in Fig. 23. The simulated fault persists for 19.5 cycles, which is the CCT with the aDPR. With the basic control, the CCT is 16 cycles. The instability is due to two SGs (G8 and G9) separating from the rest of the system. The WTG's response can be noted in Fig. 24. Although the long CCT is not as crucial for system planning as some of the faults listed in Table 2, the CCT improvement is still considerable, especially for a different type of transient instability in which a cluster of machines separate from the system. The simulations demonstrate that when an aDPR-enabled WTG is situated close to a

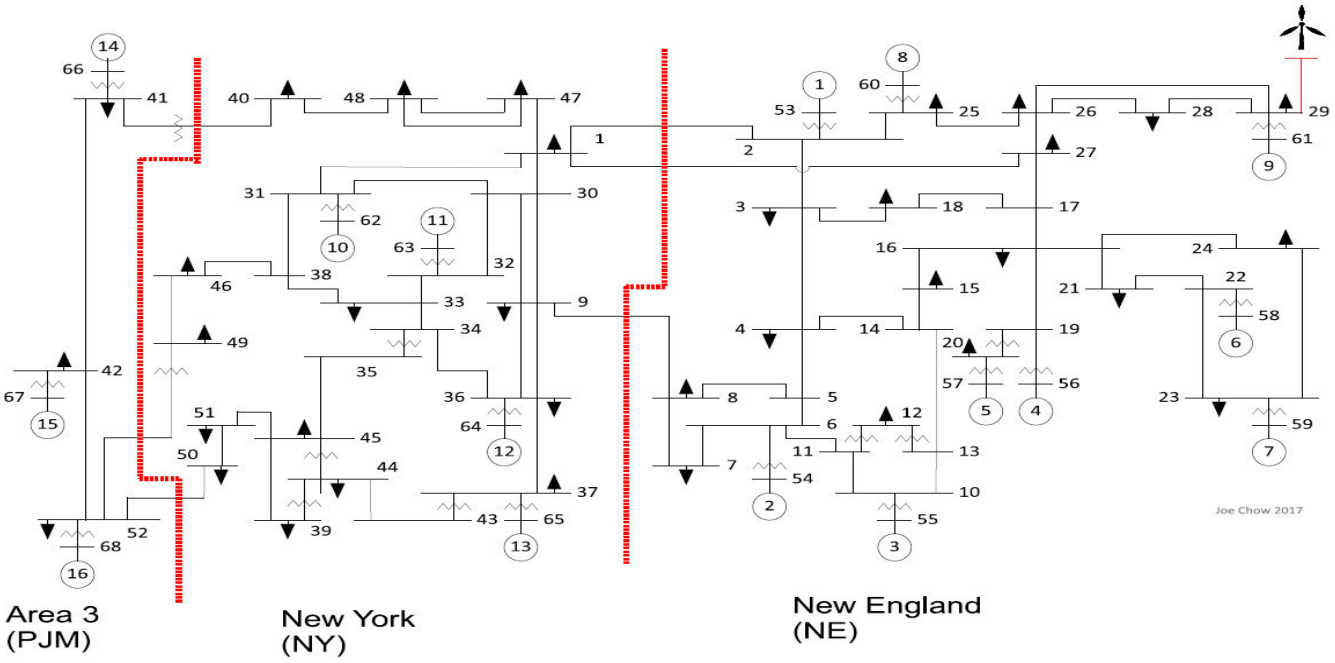

FIGURE 20. **NPCC 68-bus system.**

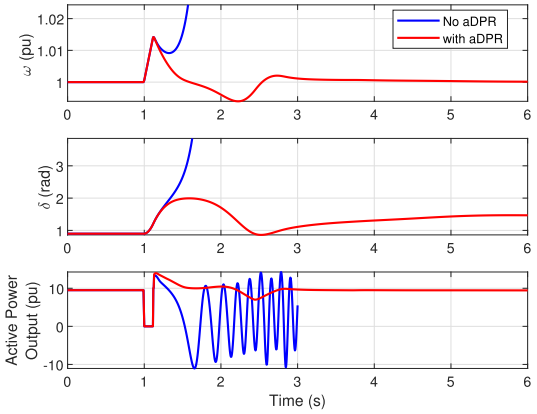

FIGURE 21. **Post-fault response of generator 9 with and without aDPR.**

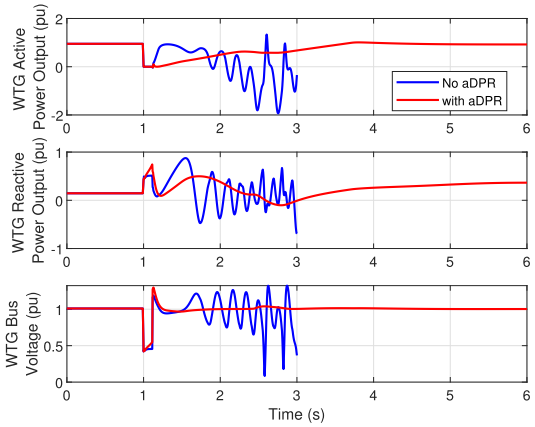

FIGURE 22. **Post-fault response of WTG with and without aDPR.**

remote SG with high power transfer towards the bulk system, it can effectively improve its transient stability, due to the effect the control has on its active power output. However, the control should not be expected to improve the stability of SGs located far away from the WTG, as the control's effect will be weaker, and due to the distance the control scheme might not even actuate. The most beneficial locations for transient stability from schemes such the aDPR can be determined via simulation and appropriate studies.

VI. TWO-AREA SYSTEM

The third system for testing the aDPR is the Kundur two-area system [31] shown in Fig. 25, with two of the 3 tie-lines present to present a more stressed condition. The dispatch is configured so Area 2 imports 400 MW from Area 1, with 200 MW from the WTG plant connected through a

TABLE 2. **CCT in cycles for different faults and load allocation with aDPR (no aDPR in parenthesis).**

Bus with Load Increase	Bus 26	Bus 27	Bus 28
Fault Line 29-28	7.2 (4.5)	7.1 (4.4)	7.2 (4.2)
Fault Line 28-29	8.4 (5.1)	8.3 (4.8)	8.3 (4.4)
Fault Line 28-26	11.1 (9)	10.9 (8.9)	12.5 (10.8)
Fault Line 26-28	9.8 (7)	9.7 (6.9)	11.6 (9)
Fault Line 29-26	8.7 (6.9)	8.6 (6.8)	9.6 (8.2)
Fault Line 26-29	9.2 (6.3)	9.1 (6.1)	10.6 (7.9)
Fault Line 26-27	11.6 (9.1)	11.4 (8.7)	12.7 (10.2)
Fault Line 27-26	16.9 (11.4)	16.4 (10.7)	19.3 (13.1)
Fault Line 25-26	19.9 (16.1)	19.9 (15.3)	19.8 (19.8)
Fault Line 26-25	11 (8.7)	10.7 (8.4)	12 (9.7)

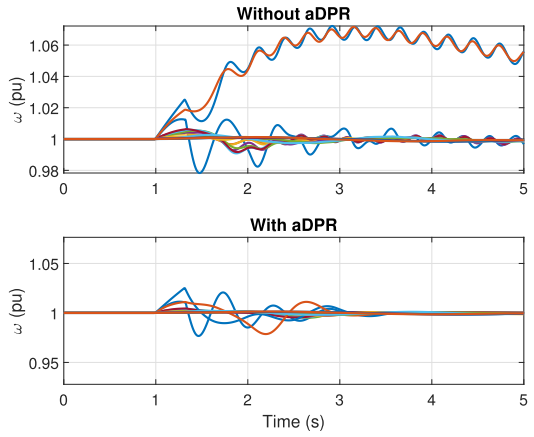

FIGURE 23. System SG speeds for fault on line 25-2.

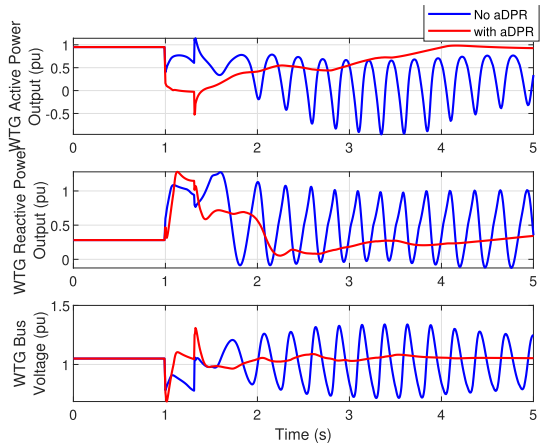

FIGURE 24. WTG response for fault on line 25-2.

sub-transmission line and a transformer to Bus 5. With only the WTG basic control, the CCT for a three-phase short-circuit fault on Bus 5, followed by a loss of a tie-line between Buses 5 and 6, is 5.1 cycles. The instability is Area 1 separating from Area 2. In order to improve the CCT, the aDPR control is enabled following the fault. For this control design, we assume the availability of frequency measurements from the boundary buses of both areas (due to observability of inter-area mode). Thus we will utilize the relative frequency of the two areas, namely, $f = f_5 - f_6$, for the aDPR control. Thus, instead of $\ddot{\gamma}$, df/dt is utilized.

The stable machine speed response for a 8.4-cycle fault is shown in Fig. 26. The aDPR stops the rotor speeds of Area 1 from further acceleration. During the disturbance, the lower voltage at Bus 6 reduces the power demand of its load, causing the rotor angles in Area 2 to advance. Thus the synchronism between the two areas is maintained. The response of the WTG is shown in Fig. 27. The aDPR ramp is tuned to 0.45 pu/s, due to the slow frequency of the interarea swing and the strong probability of second swing instabilities occurring. The PI gains have been tuned to 0.23 and 2.65, respectively. Due to the slower oscillations, the tracking of the active power

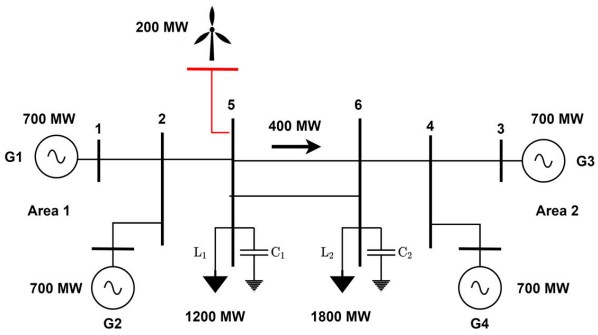

FIGURE 25. Two area Kundur system with WTG on area 1 boundary bus.

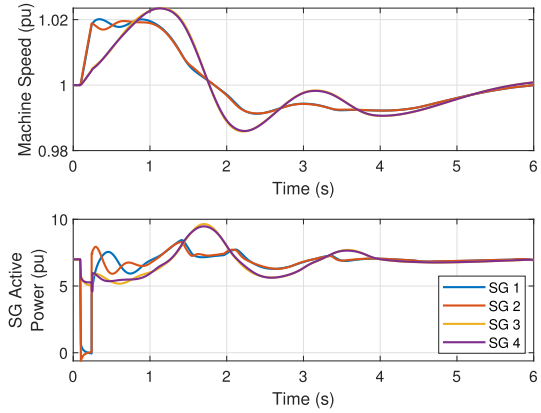

FIGURE 26. Machine speeds and active power outputs for 8.4-cycle fault.

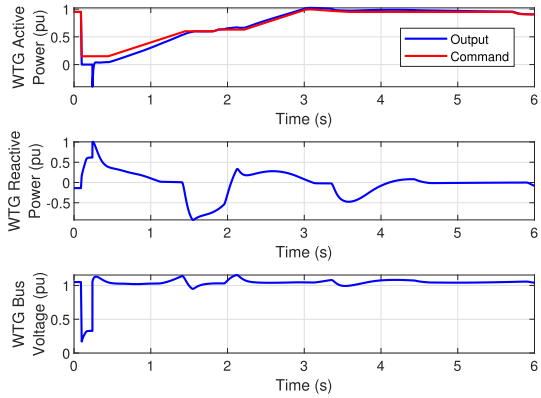

FIGURE 27. WTG active, reactive power output and terminal bus voltage for 8.4-cycle fault.

command is almost exact, especially when compared to the SMIB case. In the meantime, the reactive power damping controller is effective in damping out power oscillations on the weak tie-line. To benchmark the synchronization capability provided by the aDPR, the WTG is replaced by a SG of the same rating, equipped with a static excitation system. In addition, a 100 MVA Static Var Compensator (SVC) is

installed on Bus 5. The CCT achievable for this case is only 5.3 cycles.

VII. CONCLUSION

In this paper, a novel aDPR control for WTGs is proposed to enhance transient stability of SGs. The aDPR control consists of three components. The power reduction and ramping allows the WTG to act like a braking resistor to reduce the SG acceleration immediately following a fault. The adaptive ramping and damping control parts reduce the SG rotor deceleration and second-swing instability. In contrast to active power controls that directly commands the converter active current output, the aDRP control is implemented through the WTG active power order and setpoint. In this manner, the stress on the WTG rotor and blades is minimized by the optimization built into the WTG operation. The aDPR control is demonstrated on three systems. In each system, the WTG active power can be loaded onto existing transmission lines, thus, reducing potential transmission infrastructure investments, while the transient stability margin is improved. Further work will be directed toward coordination of aDPR control installed on multiple WTGs, to ascertain transfer capability improvement over large regions of power systems with high renewable penetration.

APPENDIX

SMIB SYSTEM PARAMETERS

The SG is represented by the transient model Parameters of the model can be found in [28]. The WTG PI damping control has parameters $K_p = 0.13$, $K_i = 1.33$ and low-pass filter time constant $T_{LP} = 0.05$ sec.

TWO-AREA SYSTEM

Parameters can be found in [31]. One tieline between buses 5 and 6 was removed and the impedance of each of the remaining lines was set to 0.22 pu. Two power system stabilizers with the machine speeds as inputs were tuned (lead compensator design) for generators 1 and 3 to achieve inter-area mode damping of 10%. Governors are also enabled on all generators.

ACKNOWLEDGMENT

This work was done while Stavros Konstantinopoulos was a Ph.D. student at Rensselaer Polytechnic Institute.

REFERENCES

[1] A. Marinopoulos, F. Papandrea, M. Reza, S. Norrga, F. Spertino, and R. Napoli, "Grid integration aspects of large solar PV installations: LVRT capability and reactive power/voltage support requirements," in *Proc. IEEE Trondheim PowerTech*, Trondheim, Norway, Jun. 2011, pp. 1–8.

[2] G. Joos, "Wind turbine generator low voltage ride through requirements and solutions," in *Proc. IEEE Power Energy Soc. Gen. Meeting-Convers. Del. Electr. Energy 21st Century*, Pittsburgh, PA, USA, Jul. 2008, pp. 1–7.

[3] B. B. Johnson, M. Sinha, N. G. Ainsworth, F. Dörfler, and S. V. Dhople, "Synthesizing virtual oscillators to control islanded inverters," *IEEE Trans. Power Electron.*, vol. 31, no. 8, pp. 6002–6015, Aug. 2016.

[4] F. Wilches-Bernal, J. H. Chow, and J. J. Sanchez-Gasca, "A fundamental study of applying wind turbines for power system frequency control," *IEEE Trans. Power Syst.*, vol. 31, no. 2, pp. 1496–1505, Mar. 2016.

[5] D. Gautam, L. Goel, R. Ayyanar, V. Vittal, and T. Harbour, "Control strategy to mitigate the impact of reduced inertia due to doubly fed induction generators on large power systems," *IEEE Trans. Power Syst.*, vol. 26, no. 1, pp. 214–224, Feb. 2011.

[6] T. D. Younkins, J. H. Chow, A. S. Brower, J. Kure-Jensen, and J. B. Wagner, "Fast valving with reheat and straight condensing steam turbines," *IEEE Trans. Power Syst.*, vol. 2, no. 2, pp. 397–403, May 1987.

[7] N. G. Hingorani and L. Gyugyi, *Understanding FACTS: Concepts and Technology of Flexible AC Transmission Systems*. New York, NY, USA: IEEE Press, 2000.

[8] C. A. Stigers, C. S. Woods, J. R. Smith, and R. D. Setterstrom, "The acceleration trend relay for generator stabilization at colstrip," *IEEE Trans. Power Del.*, vol. 12, no. 3, pp. 1074–1081, Jul. 1997.

[9] M. L. Shelton, P. F. Winkelman, W. A. Mittelstadt, and W. J. Bellerby, "Bonneville power administration 1400-MW braking resistor," *IEEE Trans. Power App. Syst.*, vol. 94, no. 2, pp. 602–611, Mar. 1975.

[10] WECC. *Wind Power Plant Dynamic Modeling Guide*. Accessed: Oct. 2021. [Online]. Available: https://www.wecc.org/Reliability/WECC%20Wind%20Plant%20Dynamic%20Modeling%20Guide.pdf

[11] J. Itai, K. Kawabe, and T. Nanahara, "Active power control of wind power generation by wide area control system for improvement of transient stability in power systems," in *Proc. 9th Int. Conf. Power Energy Syst. (ICPES)*, Dec. 2019, pp. 1–6.

[12] M. J. Morshed, "A nonlinear coordinated approach to enhance the transient stability of wind energy-based power systems," *IEEE/CAA J. Autom. Sinica*, vol. 7, no. 4, pp. 1087–1097, Jul. 2020.

[13] R. Yousefian, R. Bhattarai, and S. Kamalasadan, "Transient stability enhancement of power grid with integrated wide area control of wind farms and synchronous generators," *IEEE Trans. Power Syst.*, vol. 32, no. 6, pp. 4818–4831, Nov. 2017.

[14] A. Mitra and D. Chatterjee, "Active power control of DFIG-based wind farm for improvement of transient stability of power systems," *IEEE Trans. Power Syst.*, vol. 31, no. 1, pp. 82–93, Jan. 2016.

[15] S. Papadakis, A. Perilla, J. R. Torres, Z. Ahmad, and M. V. D. Meijden, "Real-time EMT simulation based comparative performance analysis of control strategies for wind turbine type 4 to support transient stability," in *Proc. IEEE Power Energy Soc. Gen. Meeting (PESGM)*, Montreal, QC, Canada, Aug. 2020, pp. 1–5.

[16] M. K. Hossain and M. H. Ali, "Transient stability augmentation of PV/DFIG/SG-based hybrid power system by nonlinear control-based variable resistive FCL," *IEEE Trans. Sustain. Energy*, vol. 6, no. 4, pp. 1638–1649, Oct. 2015.

[17] A. A. Eshkaftaki, A. Rabiee, A. Kargar, and S. T. Boroujeni, "An applicable method to improve transient and dynamic performance of power system equipped with DFIG-based wind turbines," *IEEE Trans. Power Syst.*, vol. 35, no. 3, pp. 2351–2361, May 2020.

[18] X. Zhao and D. Flynn, "Transient stability enhancement with high shares of grid-following converters in a 100% converter grid," in *Proc. IEEE PES Innov. Smart Grid Technol. Eur. (ISGT-Europe)*, Oct. 2020, pp. 594–598.

[19] M. Zhou, Z. Dong, H. Li, C. Gan, G. Li, and Y. Liu, "Coordinated control of DFIG based wind farms and SGs for improving transient stability," *IEEE Access*, vol. 6, pp. 46844–46855, 2018.

[20] K. Clark, N. W. Miller, and J. J. Sanchez-Gasca, "Modeling of GE wind turbine-generators for grid studies," *GE Energy*, vol. 4, pp. 0885–8950, Apr. 2010.

[21] J. H. Chow and J. J. Sanchez-Gasca, *Power System Modeling, Computation, and Control*. Hoboken, NJ, USA: Wiley, 2020.

[22] WECC REMTF. *Specification of the Second Generation Generic Models for Wind Turbine Generators*. Accessed: Oct. 2021. [Online]. Available: https://www.wecc.biz/Reliability/WECC-Second-Generation-Wind-Turbine-Models-012314.pdf

[23] N. W. Miller *et al.*, "Western wind and solar integration study phase 3A: Low levels of synchronous generation," Nat. Renew. Energy Lab. (NREL), Golden, CO, USA, Tech. Rep. NREL/TP-5D00-64822, 2015.

[24] J. H. Chow and K. W. Cheung, "A toolbox for power system dynamics and control engineering education and research,' *IEEE Trans. Power Syst.*, vol. 7, no. 4, pp. 1559–1564, Nov. 1992.

[25] F. Wilches-Bernal, J. J. Sanchez-Gasca, and J. H. Chow, "Implementation of wind turbine generator models in the power system toolbox," in *Proc. Power Energy Conf. Illinois (PECI)*, Feb. 2014, pp. 1–5.

[26] *CIGRE Technical Brochure 328: Modeling and Dynamic Behavior of Wind Generation as it Relates to Power System Control and Dynamic Performance*, CIGRE, Paris, France, Aug. 2007.

[27] F. Wilches-Bernal, C. Lackner, and J. H. Chow, "Model reduction of wind turbine generator models for control performance evaluation," in *Proc. IEEE/PES Transmiss. Distribution Conf. Expo. (T&D)*, Oct. 2020, pp. 1–5.
[28] S. Konstantinopoulos and J. H. Chow, "Dynamic active power control in type-3 wind turbines for transient stability enhancement," in *Proc. IEEE Power Energy Soc. Gen. Meeting (PESGM)*, Jul. 2021, pp. 1–5.
[29] E. V. Larsen and J. H. Chow, "SVC control design concepts for system dynamics performance," Appl. Static Var Syst. Syst. Dyn. Perform., IEEE PES Winter Meeting, New Orleans, LA, USA, IEEE PES Publication 87TH0187-5-PWR, 1987.
[30] A. K. Singh and B. C. Pal, "Report on the 68-bus, 16-machine, 5-area system," in *IEEE PES Task Force on Benchmark Systems for Stability Controls*. 2013. [Online]. Available: https://www.sel.eesc.usp.br/ieee/
[31] M. Klein, G. J. Rogers, and P. Kundur, "A fundamental study of inter-area oscillations in power systems," *IEEE Trans. Power Syst.*, vol. 6, no. 3, pp. 914–921, Aug. 1991.

STAVROS KONSTANTINOPOULOS (Member, IEEE) received the Diploma degree in electrical and computer engineering from the National Technical University of Athens, Greece, in 2015, and the M.S. and Ph.D. degrees in electrical engineering from the Rensselaer Polytechnic Institute, Troy, NY, USA, in 2018 and 2021, respectively. He is currently an Engineer II of the Grid Operations and Planning Group, Electric Power Research Institute, Palo Alto, CA, USA. His research interests include integration and control of renewable generation, transient stability analysis and control, power systems monitoring, and PMU applications.

JOE H. CHOW (Life Fellow, IEEE) received the M.S. and Ph.D. degrees from the University of Illinois at Urbana-Champaign, Champaign, IL, USA. After working in the General Electric Power System Business, Schenectady, NY, USA, he joined the Rensselaer Polytechnic Institute, Troy, NY, USA, in 1987, where he is currently an Institute Professor of electrical, computer, and systems engineering. His research interests include power systems dynamics and control, FACTS controllers, and synchronized phasor data. He is a member of the U.S. National Academy of Engineering. He was a past recipient of the IEEE PES Charles Concordia Power Engineering Award.